Geometric role in designing pneumatically actuated pattern-transforming metamaterials

Yuzhen Chen, Lihua Jin *

Department of Mechanical and Aerospace Engineering, University of California , Los Angeles, CA 90095, USA

ARTICLE INFO

ABSTRACT

When a metamaterial, composed of an elastomer with periodic circular holes sealed by elastomeric membranes, is subject to a compressive load, it can undergo a pattern transformation, yielding a large transformation strain. Such pattern transformation can be broadly tuned by changing the geometric parameters of the metamaterial. We numerically, analytically and experimentally survey the design space of the geometric parameters, and investigate their effects on the pattern transformation. Our finite element simulations reveal that the slenderest wall thickness and the pattern of the holes play key roles in determining the critical load for the pattern transformation, the transformation strain, and the transformation type. To quantify the effects of these geometric parameters, we further analytically model the pattern transformation of the metamaterial by simplifying it to a network of rigid rectangles linked by deformable beams. Finally, we experimentally characterize the pattern transformation of the metamaterials with different geometric parameters. The experimental, numerical, and analytical results are in good agreement with each other. Our work provides design guidelines for this metamaterial.

© 2018 Elsevier Ltd. All rights reserved.

1. Introduction

Mechanical metamaterials are materials with micro-architectures, which bring in unusual mechanical properties that are difficult to achieve in conventional materials [1,2]. Mechanical metamaterials with micro-/nano-lattice structures have reached unprecedentedly high stiffness and strength at an extremely low density [3,4]. Pentamode lattices have shown vanishing shear moduli [5–7]. Negative Poisson's ratio is found in auxetic metamaterials with various re-entrant structures [8–16]. In additional to the elastic constants, the whole nonlinear stress–strain relations of metamaterials are open to design. Introducing bistable structures into the micro-architectures enables pattern transformations of the metamaterials and non-monotonic stress–strain curves [17–19]. Making use of chiral lattice structures, a metamaterial can twist under a uniaxial compression [20].

Recently, a new class of mechanical metamaterials, each consisting of a rubber slab with periodic holes, has emerged [11,21–30]. These metamaterials can undergo a pattern transformation when subject to a compressive load. By harnessing the geometric nonlinearity and the pattern transformation of the metamaterials, researchers have shown a variety of unique functions of them, such as negative Poisson's ratio [11], tunable acoustic properties [30,31] and inducing torsional motions [29]. When the holes are alternatingly large and small, the stress–strain curves of the metamaterials change the monotonicity under different transverse constraints [24,26]. More interestingly, since the large and small holes collapse in two perpendicular directions, a high-symmetry square lattice of holes can transform into a low-symmetry rectangular lattice, with two energetically equivalent variants [28]. This phenomenon is analogue to the phase transformation in shape memory alloys. Indeed, the shape memory effort has been demonstrated in this kind of metamaterials [28].

The advantage of metamaterials is that their properties can be tuned by their micro-architectures [11,21,22,24–26,28]. In the metamaterials with periodic holes, the shape of the holes has been shown to tune the stiffness, Poisson's ratio, and critical condition for the pattern transformation [11,25]. The sizes of the large and small holes determine the transition between the monotonic and non-monotonic stress–strain responses [24,26]. To understand the effect of geometry on the critical condition for the pattern transformation, finite element simulations [11,21,22,25–28,32,33] and analytical models [32,33] have been developed for the metamaterials with uniform-sized holes. These analytical models can predict the critical condition for the pattern transformation based on buckling analysis of the slender ligaments. However, they fail to predict the transformation strains due to lack of post-buckling analysis. For the metamaterials with alternatingly large and small holes, an analytical model has been proposed to understand the programmable monotonicity of the stress–strain curves [24]. However, this model is simple and unable to capture the geometric effects.

---

* Corresponding author.
E-mail address: lihuajin@seas.ucla.edu (L. Jin).
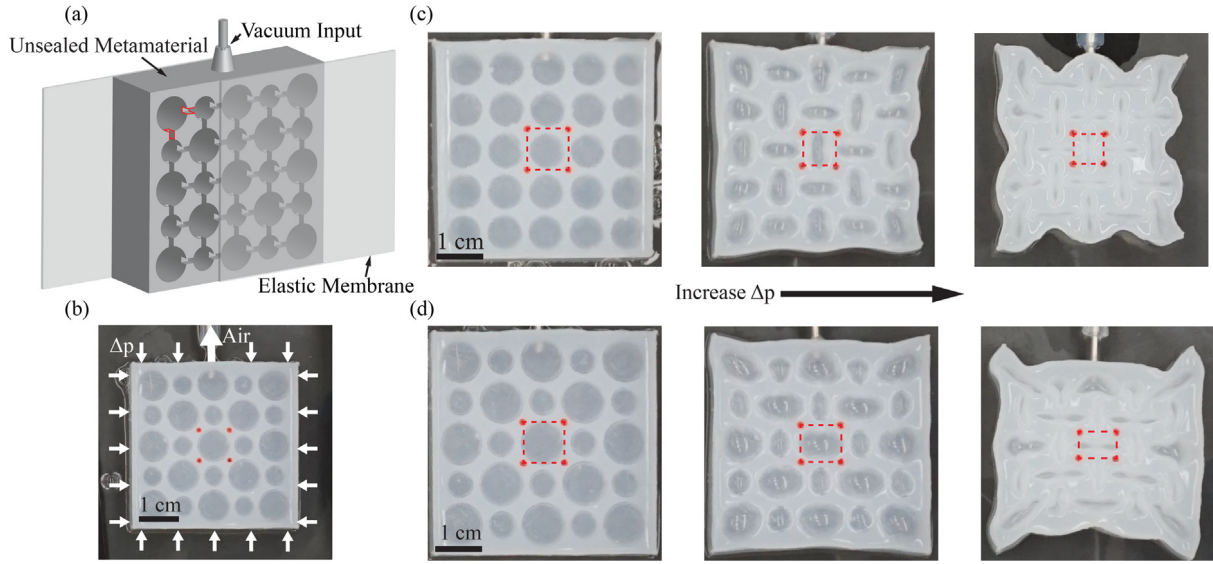
Fig. 1. Overview of the pneumatically actuated pattern-transforming metamaterials. (a) A schematic of the fabrication. The metamaterial is an elastomeric slab containing an array of holes. All the holes are sealed by two elastic membranes, isolating the inner air from the atmosphere. The air chambers formed by the holes are connected via grooves (two of which are outlined in red). The metamaterial is actuated by a source of vacuum, such as a syringe or a pump. (b) When actuated, the metamaterial is subjected to an external and internal pressure difference and undergoes a pattern transformation. (c) When the holes are uniform-sized, the square lattice keeps square and the transformation strain is equibiaxial. (d) When the holes are alternatingly large and small, the square lattice transits to a rectangular shape and the transformation strain is non-equibiaxial.

In this paper, combining finite element analysis, experiments and analytical modeling, we aim to establish quantitative understanding and a predictable theory to unravel the effects of geometry on the mechanical behavior of the metamaterials with arbitrary sizes of the alternatingly large and small holes. In experiments, to better control the deformation, we design and fabricate pneumatically actuated metamaterials, as illustrated in Fig. 1a, where an elastomeric slab patterned with a square array of holes is sealed by two thin elastomeric membranes. Narrow and shallow grooves are used to connect all the holes so that air can flow freely throughout the whole structures. The holes are further linked to an external source of vacuum via a tube (Fig. 1b). At a critical pressure Δp_{cr}, with Δp defined as the difference between the external and internal pressures, $\Delta p = p_{ext} - p_{int}$, the metamaterial undergoes a pattern transformation with the circular holes altering their shapes into ellipses orthogonal to their neighbors, yielding a large transformation strain (Fig. 1c–d). The pattern transformation, and therefore the corresponding transformation strain, is widely tunable: the pattern of uniform-sized holes leads to an equibiaxial contraction (Fig. 1c), whereas the pattern of alternatingly large and small holes leads to a non-equibiaxial contraction (Fig. 1d). We will numerically and experimentally characterize the pattern transformation as a function of the pressure Δp, and explore the effect of a wide range of geometric parameters. We will further provide an analytical model to explain how the geometry affects the pattern transformation of the metamaterials.

The paper is organized as follows. In Section 2, we perform finite element simulations to investigate the tunable pattern transformation of the metamaterial by surveying the design space of the geometric parameters. In Section 3, we develop an analytical model to understand the effect of geometry on the critical condition for the pattern transformation, the transformation strain and the transformation type. Finally, we conduct experiments in Section 4 to demonstrate the tunable pattern transformation of the metamaterials and verify the results of the finite element simulations and the analytical model. Section 5 will conclude the paper.

2. Finite element analysis

In this section, we systematically investigate the role of geometry in determining the critical pressure, transformation strain and the transformation type using finite element simulations in Abaqus (version 6.14).

We perform simulations in a unit cell of an elastomeric slab (Fig. 2a), which is selected as the smallest geometric unit that can build up the whole system by mirroring and patterning itself [34]. Symmetric boundary conditions are applied to the unit cell, i.e., on the bottom and left boundaries displacement is only allowed in the horizontal and vertical directions, respectively, and the top and right boundaries are constrained to maintain horizontal and vertical, respectively (Fig. 2b). Although these boundary conditions are not periodic, a 2×2 cell, by mirroring the current unit cell horizontally and vertically, is equivalent to the smallest repeated structure for the periodic boundary condition. Besides, the unit cell is subjected to a pressure Δp on all the surfaces of the holes. The geometric parameters of the unit cell include the two radii R and r, and the lattice size L, the subtraction of which defines the thickness of the slenderest wall, $t = L - R - r$. We normalize the geometric parameters by the lattice size L and obtain two independent dimensionless parameters: R/L and r/L. We model the elastomer as an incompressible neo-Hookean continuum solid, whose strain energy density function W is given as [35,36]

$$W = \frac{\mu}{2}\left(tr\left(\mathbf{FF}^{\mathrm{T}}\right) - 3\right) \tag{1}$$

where μ is the shear modulus, and $\mathbf{F}$ is the deformation gradient tensor with the constraint $\det(\mathbf{F}) = 1$. We use eight-node, quadratic, hybrid, plane strain elements (ABAQUS element type CPE8H), and perform mesh refinement study to ascertain the accuracy of simulations. To break the symmetry, small imperfections with amplitude $\sim t/1000$ are introduced to the initial coordinates of the nodes. We simulate the deformation of the unit cell under the pressure based on the Riks method, and calculate the strains ε_x and ε_y, defined as the changes in length of the lattice with respect to the original length in the x and y directions (Fig. 2c).

Fig. 3 shows the simulation results of the strain–pressure relations (Fig. 3a, b) and the shape evolution of four unit cells of
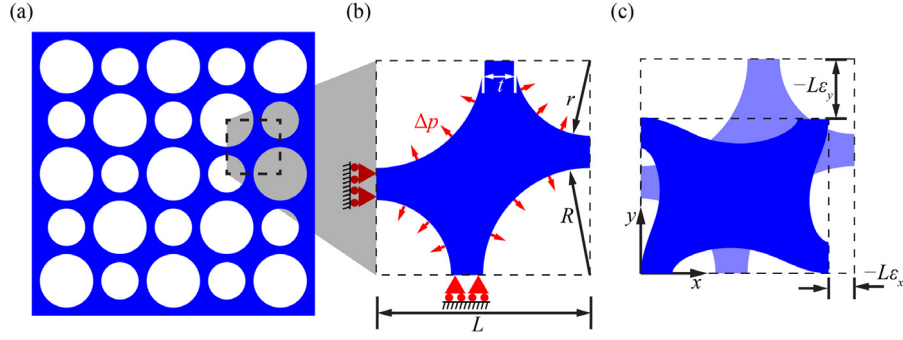
Fig. 2. The setup of the finite element simulations. (a) A schematic of an elastomeric slab composed of an array of holes. (b) The unit cell used for the finite element simulations. A unit cell is identified here as the smallest geometric unit that can build up the whole system by mirroring and patterning itself. This unit cell is constrained by the symmetric boundary conditions, and is subjected to a pressure Δp, defined as the difference between the external pressure p_{ext} and the internal pressures p_{int} ($\Delta p = p_{ext} - p_{int}$). The geometric parameters include the two radii R and r, and the lattice size L, which define two dimensionless geometric parameters. (c) The deformation of this unit cell is measured by changes in length of the lattice in the x and y directions between the undeformed state (light blue) and deformed state (dark blue). (For interpretation of the references to color in this figure legend, the reader is referred to the web version of this article.)
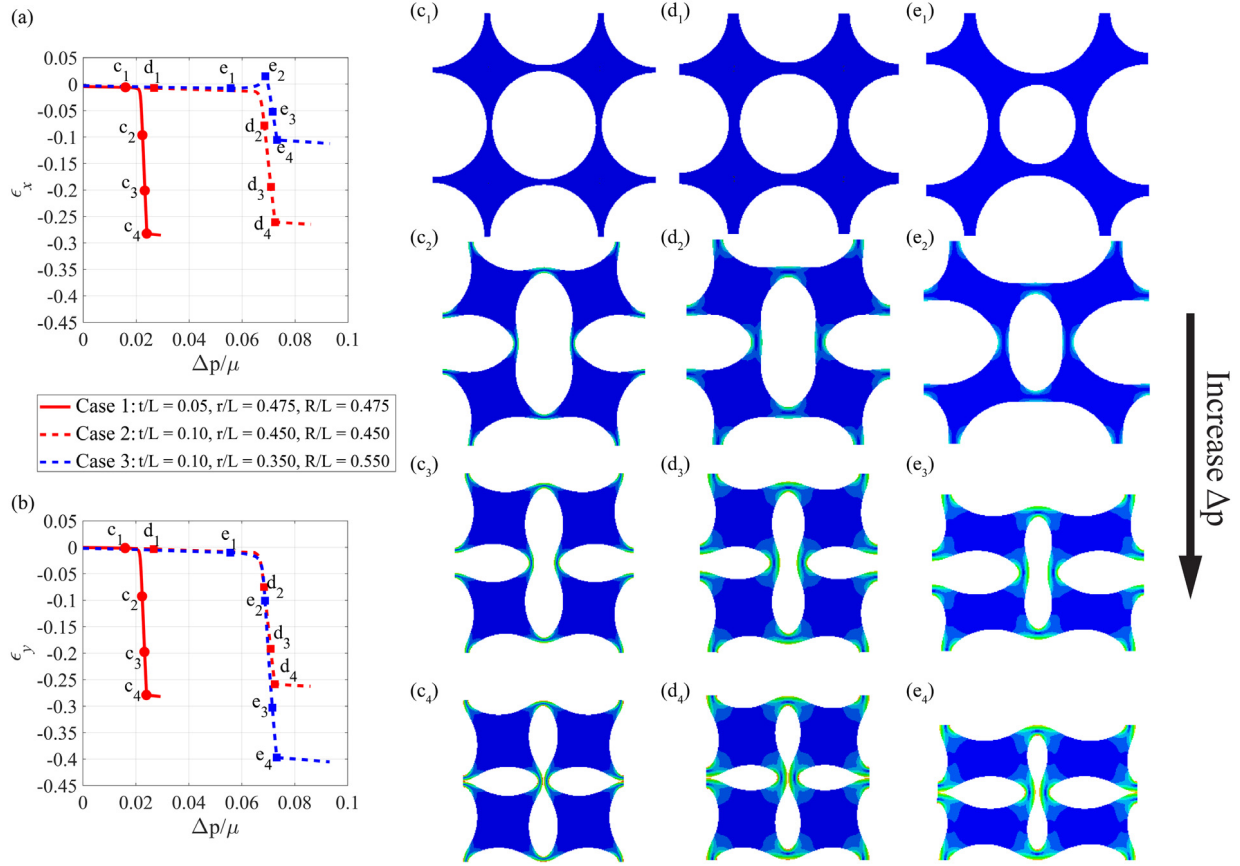

Fig. 3. The results of the finite element simulations for three metamaterials with different geometric parameters. The dependence of the strains in the (a) x and (b) y directions on the pressure. (c)–(e) The deformed shapes of four unit cells of the three metamaterials: (c) uniformly large holes ($r/L = R/L = 0.475$, $t/L = 0.05$), (d) uniformly small holes ($r/L = R/L = 0.450$, $t/L = 0.10$), and (e) alternatingly large and small holes ($r/L = 0.350$, $R/L = 0.550$, $t/L = 0.10$). For each case, the states of the deformation correspond to the four selected points on its strain–pressure curves.

three metamaterials with different geometric parameters: uniformly large holes (Fig. 3c), uniformly small holes (Fig. 3d), and alternatingly large and small holes (Fig. 3e). For all cases, when the pressure is small, both strains ε_x (Fig. 3a) and ε_y (Fig. 3b) only slightly decrease as the pressure increases. After the pressure reaches a critical value, the strains sharply drop, indicating a pattern transformation occurs. The deformed shapes of the metamaterials under different pressures shown in Fig. 3c–e correspond to the points marked on the strain–pressure curves in Fig. 3a, b. The

strain–pressure curves reach another almost flat stage when the metamaterials form internal contact (Fig. 3c$_4$–e$_4$).

Apart from these common features, we observe that the geometry can significantly affect the critical pressure and the transformation strains. Smaller holes, and therefore a larger wall thickness, lead to a higher critical pressure ($r/L = R/L = 0.475$, $t/L = 0.05$ for Fig. 3c, and $r/L = R/L = 0.450$, $t/L = 0.10$ for Fig. 3d). Interestingly, although the pattern of the holes in Fig. 3e ($r/L = 0.350$, $R/L = 0.550$, $t/L = 0.10$) is different from that in Fig. 3d, the two cases have the same critical pressure due to
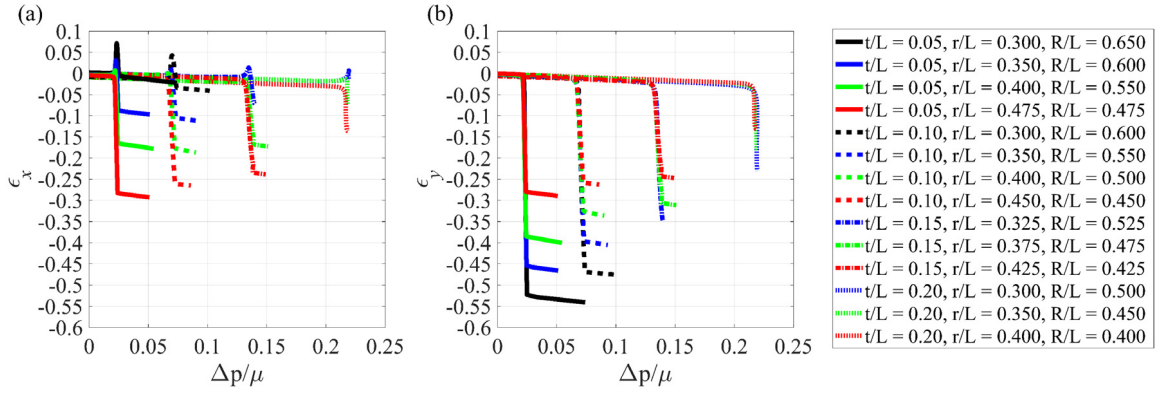
Fig. 4. The dependence of the strains in the (a) *x* and (b) *y* directions on the pressure for fourteen sets of geometric parameters. The critical pressure for the onset of pattern transformation is shown to be governed by the wall thickness *t/L*.

the same wall thickness. When the holes are uniform-sized ($r = R$), the transformation strain is equibiaxial, i.e. $\varepsilon_x = \varepsilon_y$, and the square lattice keeps a square shape. In contrast, when the holes are alternatingly large and small ($r \neq R$), the transformation strain is non-equibiaxial, i.e. ε_x and ε_y bifurcate from each other after the pressure reaches its critical value, and the square lattice transits to a rectangular shape. The three cases discussed have shown the fact that the pattern transformation of these metamaterials can be tuned by varying the wall thickness and the pattern of the holes.

Next, we survey the space of the geometric parameters and demonstrate the wide tunability of the pattern transformation. Fig. 4 presents the strain–pressure curves for fourteen sets of geometric parameters. These sets can be sorted into four groups according to the value of the wall thickness: $t/L = 0.05$, $t/L = 0.10$, $t/L = 0.15$, and $t/L = 0.20$, represented by four different types of lines. These curves clearly show that the wall thickness determines the critical pressure, no matter whether the neighboring holes have the same size or not, and the critical pressure increases with the wall thickness. We also observe that the pattern of the holes determines the biaxiality of the transformation strain. As the ratio of the small radius to the large radius, r/R, decreases, the transformation strain deviates more from an equibiaxial contraction. When $r/L = 0.3$ and $R/L = 0.65$ (the black solid curve in Fig. 4), the transformation strain is almost uniaxial with ε_y over 0.52 and ε_x less than 0.003 when the internal contact occurs. Note that the ε_x-pressure curves for metamaterials with alternatingly large and small holes always have overshoots (Fig. 4a), i.e. ε_x becomes positive prior to the sharp drop during the pattern transformation, while these overshoots do not occur for metamaterials with uniform holes. These overshoots are caused by the competition between the extension in the *x* direction when the unit cells tilt down and the contraction in the *x* direction in response to the pressure, occurring in metamaterials with unequal radii of neighboring holes. At the beginning of the pattern transformation, the extension caused by rotation of the unit cells dominates the change in strain ε_x. As the pressure increases, the contraction wins, and ε_x sharply decreases. For the metamaterials with uniform holes, however, no overshoot exists. This is because their unit cells are enclosed in the inscribed circle of the initial lattice, and thus the unit cells are unable to exceed the boundary of the initial lattice while tilting down. Instead, they are compressed into a smaller lattice under an increasing pressure, leading to a monotonic decrease in both strains ε_x and ε_y during the pattern transformation. Moreover, as the wall thickness t/L increases, the transformation type varies from a continuous second-order transition to a discontinuous first-order transition. When the wall thickness is small ($t/L = 0.05$, 0.10, or 0.15), the strains continuously, although sharply, drop as the pressure increases during the pattern transformation. However, when the wall thickness is large ($t/L = 0.20$), the slopes

of the pressure–strain curves become positive (corresponding to negative slopes of the stress–strain curves) at the critical pressure, which indicates a discontinuous drop of the strains.

In this section, we have performed finite element simulations for a wide range of geometric parameters. From the results, we conclude that the pattern transformation of these metamaterials can be tuned by their geometry. To understand the role of the geometric parameters in governing the mechanics of the pattern transformation, an analytical model is proposed in the next section.

3. Analytical model

3.1. Formulation of the analytical model

Fig. 5a is a typical contour plot of the maximal principle logarithmic strain in four unit cells of a metamaterial ($t/L = 0.05$, $r/L = 0.350$, and $R/L = 0.600$) under a pressure $\Delta p/\mu = 0.0246$ larger than the critical pressure for the pattern transformation. The result shows that the deformation is mainly concentrated in the slender regions, whereas the rest regions (shown in blue) only deform by less than 2%. Therefore, we propose to simplify the slender regions as deformable beams, and the nearly undeformed regions as rigid rectangles [32], yielding a simplified structure as sketched in Fig. 5b. By modeling the buckling and post-buckling of this simplified structure, we are able to analytically calculate the strain–pressure relations of the metamaterials.

The unit cell in the simplified structure is characterized by the dimension of the rigid rectangles ($a \times b$) and the dimension of the deformable beams ($2h \times w$) (Fig. 5b). We set the boundaries of the rigid rectangles tangent to the neighboring circular holes, and set the thickness *w* of the deformable beams equal to the wall thickness *t*. To smoothly transit from the rigid rectangles to the deformable beams, the length of the deformable beams $2h$ is chosen to be longer than the distance between the two corners of the rigid rectangles by *w*, which takes into account the boundary effect of bending of the slender regions on the rectangles (Fig. 5b). As a result, we can relate the geometric parameters of the metamaterials to those of the simplified structures:
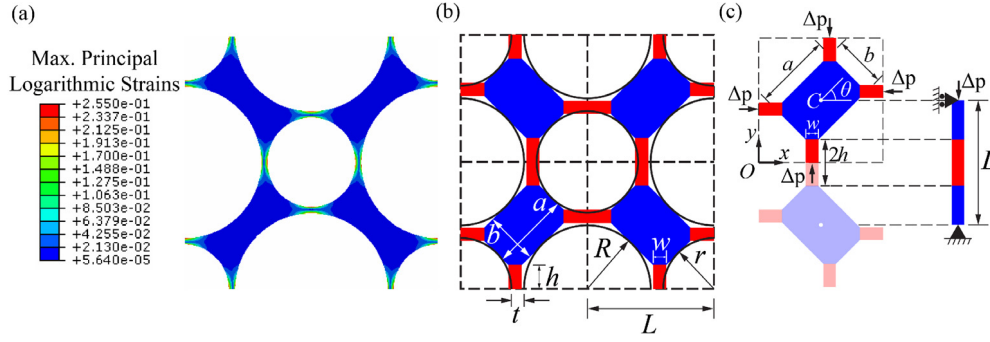
$$a = \sqrt{2}L - 2r, \tag{2}$$

$$b = \sqrt{2}L - 2R, \tag{3}$$

$$w = t, \tag{4}$$

$$h = \frac{L}{2} - \frac{\sqrt{2}}{4}a - \frac{\sqrt{2}}{4}b + \frac{t}{2} = \frac{\sqrt{2}-1}{2}(L-t), \tag{5}$$

Fig. 5. Sketches of the simplified structure and the equivalent one-dimensional beam model. The contour plot (a) of the maximal principal logarithmic strain for a metamaterial with geometric parameters $t/L = 0.05$, $r/L = 0.350$, and $R/L = 0.600$ at loading $\Delta p/\mu = 0.0246$ shows that the deformation mainly concentrates in the slender regions. Thus, we proposed (b) a simplified structure consisting of rigid rectangles (blue) linked by deformable beams (red). The black solid line denotes the outlines of the holes, to which the edges of the blue parts are tangent. (c) To analytically determine the pattern transformation of this simplified structure, we solve the buckling and post-buckling behavior of an equivalent one-dimensional model composed of a deformable beam fixed to two rigid bars subject to an axial compressive stress Δp. (For interpretation of the references to color in this figure legend, the reader is referred to the web version of this article.)

where we have used $L = r + R + t$. Eq. (5) means that the length of the deformable beams, h/L, depends solely on the wall thickness t/L. With Eqs. (2)–(5), we can convert the metamaterial into a simplified structure, which maintains the main features of pattern transformation (See verification by finite element analysis in Fig. A.1).

Next, we will analytically quantify the pattern transformation of this simplified structure. We will solve its buckling condition, which gives rise to the critical pressure for the pattern transformation. By further formulating its post-buckling process, we will analytically determine the strain–pressure relations during the pattern transformation.

The buckling and post-buckling of this simplified structure can be determined in an equivalent one-dimensional model composed of a beam with length $l_s = 2h$ fixed to two rigid bars with length $l_r = (L - l_s)/2$ subject to an axial compressive stress Δp, as shown in the right of Fig. 5c and Fig. 6a. In a unit cell of a metamaterial with alternatingly large and small holes, although the two vertical loads offset by a distance, creating a moment about the center C of the rigid rectangle, the moment is balanced by that created by the two horizontal loads. Thus, shifting the deformable beams to the vertical and horizontal lines past the center C does not change their buckling and post-buckling behavior (Fig. 5c). Moreover, since the rigid rectangles are free to rotate and translate during the pattern transformation, the equivalent beam model is restrained by a pin-roller support.

The buckling and post-buckling behavior of this beam model (Fig. 5c, 6a) under the plane strain condition are solved analytically based on Euler's elastica and the theory of elastic stability [37] (see the derivation in Appendix B). The beam is assumed to be linearly elastic with the Young's modulus E, Poisson's ratio $\nu = 0.5$, and shear modulus $\mu = E/3$. It is considered inextensible in the buckling and post-buckling analysis, because the compressive strain in response to the axial load is negligible compared to the displacement caused by the buckling. The beam buckles when the axial compressive force $N = \Delta pw$ reaches its critical value N_{cr}, which can be obtained by solving the following equation:

$$2k_{cr}l_r \cos k_{cr}l_s = \left(k_{cr}^2 l_r^2 - 1\right) \sin k_{cr}l_s, \tag{6}$$

where $k_{cr} = \sqrt{N_{cr}/K}$ and $K = Ew^3/\left[12\left(1 - \nu^2\right)\right]$ is the bending stiffness of the beam in the plain strain condition. Note that the critical force N_{cr} recovers that of a simply supported beam when $l_r = 0$. The existence of the rigid bars (non-zero l_r) can significantly reduce the critical buckling force of a beam fixed to two rigid bars.

As the load N slightly exceeds the critical value N_{cr}, the beam buckles, and its deflection v is given by

$$v(x) = a \sin(k_{cr}x + \gamma), \tag{7}$$

where the coordinate x is chosen to be along the tangential direction of the beam (Fig. 6a), $\tan \gamma = k_{cr}l_r$, and the amplitude a as a function of N is given by

$$a = \frac{1}{2k_{cr}} \sqrt{\frac{N - N_{cr}}{N_{cr}} \frac{32l_s\left(1 + k_{cr}^2 l_r^2\right)^2 + 64l_r\left(1 + k_{cr}^2 l_r^2\right)}{l_s\left(1 + k_{cr}^2 l_r^2\right)^2 + 2l_r\left(1 - k_{cr}^2 l_r^2\right)}}. \tag{8}$$

The bending angle $\varphi(x)$ is solved as

$$\varphi(x) = \sin^{-1}\left(v'(x)\right) = \sin^{-1}\left(ak_{cr}\cos\left(k_{cr}x + \gamma\right)\right). \tag{9}$$

Using the assumption of the inextensible beam, we obtain the axial shortening of the beam Δl_s,

$$\Delta l_s = \int_0^{l_s} \left(1 - \sqrt{1 - v'^2}\right) dx \approx \int_0^{l_s} \frac{1}{2}v'^2 dx$$
$$= \frac{a^2 k_{cr}^2 \left(l_s + k_{cr}^2 l_r^2 l_s - 2l_r\right)}{4\left(1 + k_{cr}^2 l_r^2\right)}. \tag{10}$$

The length change of the whole structure ΔL involves the contributions from the beam and the rigid bars, which yields
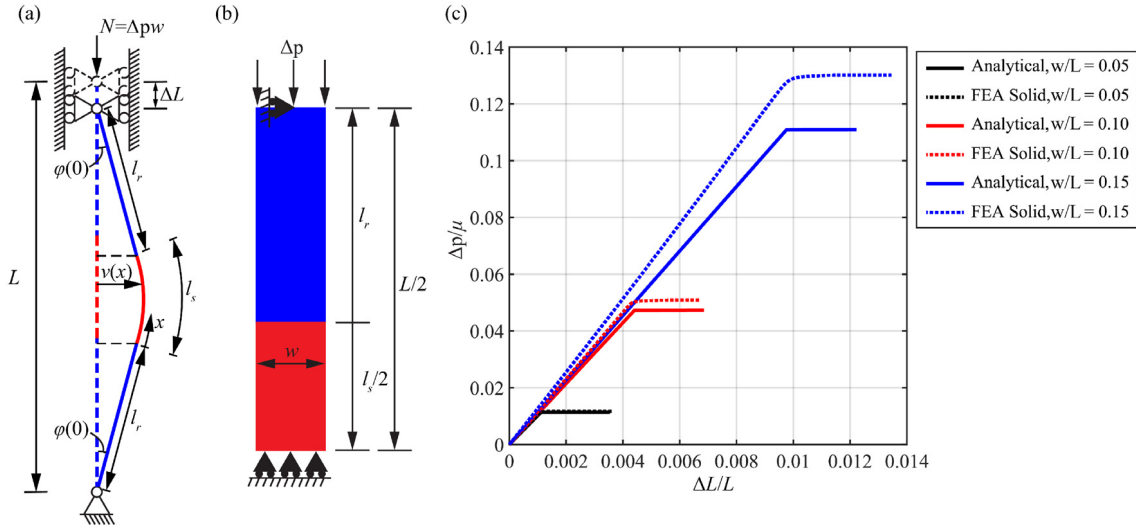
$$\Delta L = \Delta l_s + 2l_r\left(1 - \sqrt{1 - v'(0)^2}\right). \tag{11}$$

To verify the above analytical buckling and post-buckling solutions of the beam model, we perform finite element analysis using solid elements (Abaqus element type CPE8H) with the load and boundary conditions sketched in Fig. 6b. The results are compared with the analytical solutions for different width-to-length ratios w/L (Fig. 6c). Note that according to Eq. (5), w/L uniquely determines h/L, and therefore l_s/L and l_r/L. As a result, the critical displacements from the analytical solutions and the simulations are in good agreement, which verifies our analytical solutions. The critical load from the finite element simulations is slightly higher than that from the analytical solutions, because in the simulations the rigid bars constrain the lateral expansion of the beam near their interfaces, increasing the effective stiffness of the beam, which is not accounted in the analytical beam model.

With this equivalent beam model, we are able to determine the pattern transformation of the simplified structure. The critical Δp_{cr} for the pattern transformation is given by

$$\Delta p_{cr} = \frac{N_{cr}}{w}, \tag{12}$$

where N_{cr} is the buckling load for the beam in Eq. (6). The critical pressure Δp_{cr} only depends on the thickness of the slenderest wall t/L, since t/L uniquely determines the lengths of the beam

Fig. 6. Buckling and post-buckling analysis of the one-dimensional beam model. (a) The model consists of a beam (red) of length $l_s = 2h$ fixed to two rigid bars (blue) of length $l_r = (L - l_s)/2$. The whole structure is simply supported at the two ends, and is subject to an axial load N. When the load exceeds a critical value, the beam buckles, deviating from its initial straight position (dashed line), with the deflection $v(x)$ and bending angle $\varphi(x)$. (b) To verify our analytical buckling and post-buckling solutions, we perform finite element analysis (FEA) using solid elements. (c) The pressure–displacement relations for different width-to-length ratios w/L from the analytical solutions and the FEA using solid elements show good agreement. (For interpretation of the references to color in this figure legend, the reader is referred to the web version of this article.)

$l_s/L = 2h/L$ and the rigid bars l_r/L. When Δp is lower than the critical stress Δp_{cr}, the orientation of the rigid rectangle θ (Fig. 5c) keeps 45° without a rotation, and the contraction of the unit cell is purely due to the deformation of the elastic beams. Consequently, the strains and the coordinates of the center point $C(x_c, y_c)$ are given by

$$\begin{cases} \epsilon_x = -\dfrac{2(1 - \tilde{v}^2) h}{3L} \dfrac{\Delta p}{\mu}, \\ \epsilon_y = -\dfrac{2(1 - \tilde{v}^2) h}{3L} \dfrac{\Delta p}{\mu}, \end{cases} \quad \begin{cases} x_c = \dfrac{L}{2}(1 + \epsilon_x), \\ y_c = \dfrac{L}{2}(1 + \epsilon_y), \end{cases} \quad (13)$$

where the origin is taken as the bottom left corner point of the unit cell (Fig. 5c). When Δp exceeds the critical stress Δp_{cr}, all the beams in a unit cell buckle clockwise (or counter-clockwise) due to the constraint of the rigid rectangle. The rigid rectangle rotates following the buckled beams with the orientation decreases (or increases) by $\Delta\theta$ equal to the bending angle of the beams at the ends $\varphi(0)$ determined in Eq. (9). Considering the current orientation angle of the rigid rectangle $\theta = 45° - \varphi(0)$, and the axial displacement of the beam Δl_s in Eq. (10), we can derive the strains of the unit cell and the coordinate of the center $C(x_c, y_c)$ as functions of Δp as following

$$\begin{cases} x_c = h - \dfrac{\Delta l_s}{2} + \dfrac{a}{2}\cos\theta + \dfrac{b}{2}\sin\theta - \dfrac{w}{2}\cos\varphi(0), \\ y_c = h - \dfrac{\Delta l_s}{2} + \dfrac{a}{2}\sin\theta + \dfrac{b}{2}\cos\theta - \dfrac{w}{2}\cos\varphi(0), \end{cases}$$

$$\begin{cases} \varepsilon_x = \dfrac{2}{L}x_c - 1, \\ \varepsilon_y = \dfrac{2}{L}y_c - 1, \end{cases} \quad (14)$$

where the first two terms of the coordinate x_c or y_c represent the half length of a beam in the x or y direction respectively, and the last three terms of the coordinate x_c or y_c represent the contribution of the rigid rectangle in the x or y direction respectively (Fig. 5c). The evolution of the pattern transformation slows down when the beams form contact with each other. The contact occurs when the bottom beam sketched in the unit cell in Fig. 5c reaches the y axis

or the right beam reaches the x axis, yielding correspondingly

$$\begin{cases} x_c - \dfrac{a}{2}\cos\theta + \dfrac{b}{2}\sin\theta + \dfrac{w}{2}\sin\varphi(0) - (v(h) - v(0)) - \dfrac{w}{2} = 0, \\ \qquad\qquad\qquad OR \\ y_c + \dfrac{a}{2}\sin\theta - \dfrac{b}{2}\cos\theta + \dfrac{w}{2}\sin\varphi(0) - (v(h) - v(0)) - \dfrac{w}{2} = 0, \end{cases} \quad (15)$$

where the first four terms in the first or second equation are the x or y coordinate of the end of the bottom or the right beam where it connects to the rigid rectangle, the fifth term in the parentheses is the relative deflection at the midpoint of the beam with respect to its end, and the last term defines the distances between the neutral axis and the surface of the beam. The deflections v of the buckled beam as a function of Δp is given by Eqs. (7) and (8). Eq. (15) determines the critical Δp when the contact forms, and the corresponding strains can be calculated by Eq. (14). Combining Eqs. (12)–(15), we can analytically obtain the pattern transformation of the simplified structure with different geometric parameters.

3.2. Results of the analytical model

Fig. 7 shows the prediction of the pattern transformation based on the analytical model for metamaterials with three sets of geometric parameters same as those in Fig. 3 (case 1, uniformly large holes; case 2, uniformly small holes; and case 3, alternatingly large and small holes). The results of our analytical model agree with those from the finite element simulations in Fig. 3. When the pressure is small, the strains in the x and y directions, ε_x (Fig. 7a) and ε_y (Fig. 7b), do not change significantly as the pressure increases. When the pressure Δp reaches a critical value Δp_{cr}, the beams buckle and initiate the pattern transformation (Fig. 7 c_1–e_1). Since the case 1 has thinner beams, its pattern transformation initiates earlier than those of the cases 2 and 3. With the equal beam thickness, the pattern transformations in the cases 2 and 3 initiate at the same critical pressure, governed by the buckling condition of the beams. As the pressure further increases, the transformation strains sharply drop in all the three cases (Fig. 7a, b). When the holes are uniform-sized ($r = R$), the transformation strain is equibiaxial (Fig. 7a, b), and the square lattice remains a square shape (Fig. 7c–d), whereas when the holes are alternatingly large and small ($r \neq R$), the transformation strain is non-equibiaxial
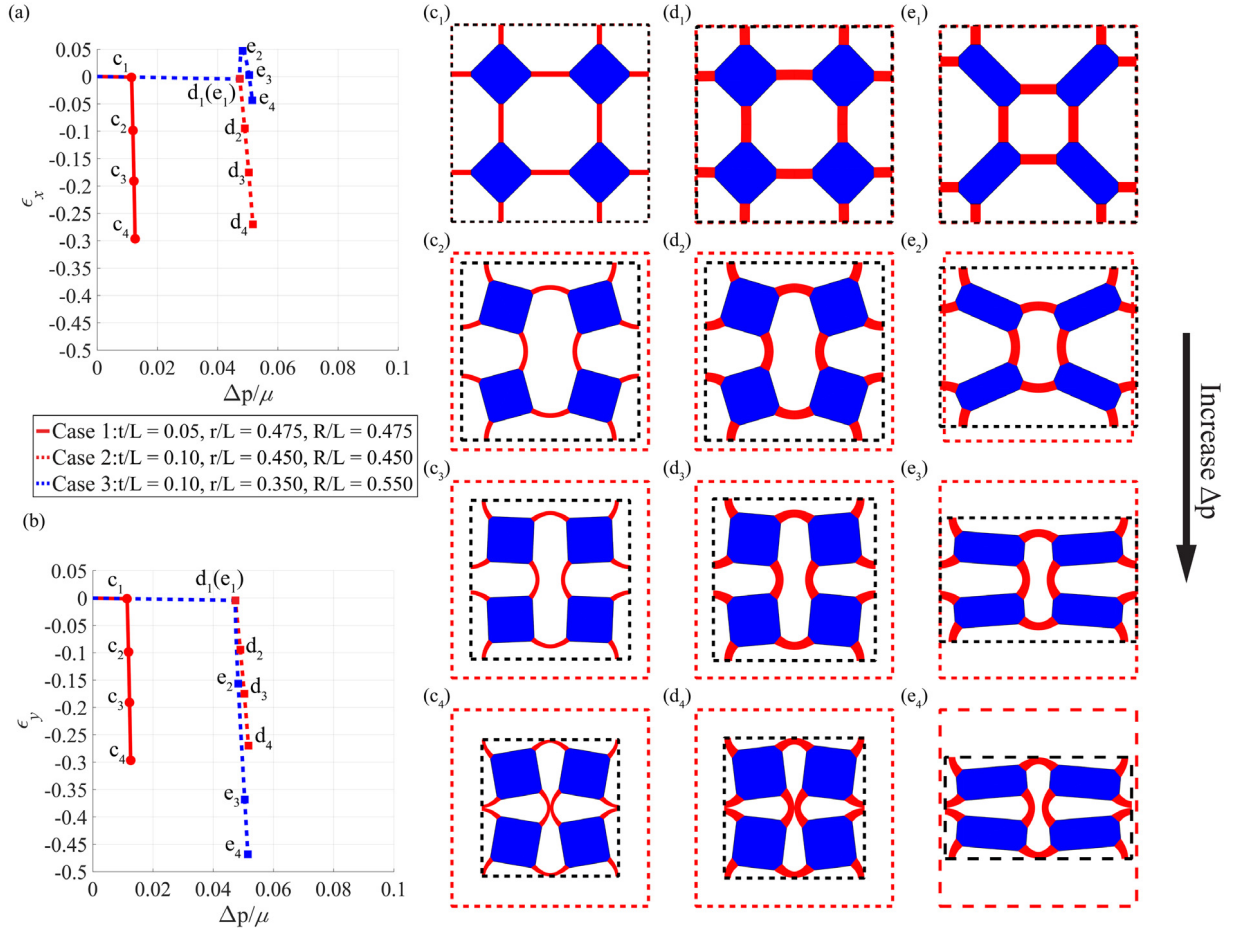
Fig. 7. The prediction of the pattern transformation based on the analytical model for metamaterials with three different sets geometric parameters same as those in Fig. 3. The dependence of the strains in the (a) x and (b) y directions on the pressure. (c)–(e) The deformed shapes of four unit cells of the three metamaterials: (c) uniformly large holes ($r/L = R/L = 0.475, t/L = 0.05$), (d) uniformly small holes ($r/L = R/L = 0.450, t/L = 0.10$), and (e) alternatingly large and small holes ($r/L = 0.350, R/L = 0.550, t/L = 0.10$). For each case, the states of deformation correspond to the four selected points on its strain–pressure curves. The red dashed frames denote the initial boundaries of the lattice, whereas the black dashed frames represent the current boundaries of the lattice. (For interpretation of the references to color in this figure legend, the reader is referred to the web version of this article.)

(Fig. 7a, b), and the square lattice transits to a rectangular shape (Fig. 7e) (see Videos S1–3 in Appendix D).

We now apply our analytical model to metamaterials with other geometric parameters. We restrict ourselves to thin beams ($t/L \leq 0.15$) because Euler's elastica fails to capture the post-buckling behavior for wide beams [38]. In particular, when the width-to-length ratio is high, the slope of the pressure–displacement curve (Fig. 6c) has been shown to be negative [38], which is consistent with our finite element prediction that the pattern transformation becomes discontinuous when the wall thickness is large (Fig. 4). In Fig. 8, we plot the strain–pressure curves for eleven sets of geometric parameters. Our analytical model can capture all the features observed in the finite element simulations. (i) The critical pressure Δp_{cr} is governed by and increases with the wall thickness. (ii) The patterns of the holes control the biaxiality of the transformation strain. (iii) When the holes are alternatingly large and small, an overshoot exists in the $\varepsilon_x - \Delta p$ curves, i.e. ε_x first increases and then decreases as Δp increases at the onset of the pattern transformation, whereas no overshoot exists when the holes are uniform-sized.

4. Experimental results

To experimentally verify the role of the geometric parameters on the pattern transformation of the metamaterials, we fabricated metamaterials with different geometric parameters and measured

the strains as functions of the external and internal pressure difference. The samples, each with lateral dimensions of 50 mm by 50 mm and thickness of 25 mm, were made of Ecoflex 00–30 (shear modulus $\mu = 30$ KPa [39]) and fabricated by casting the elastomer precursor into a 3D printed mold. We used the same Ecoflex as a glue to seal the holes with two thin membranes on the front and back sides of the slab (Fig. 1a). Shallow groove structures were designed into the metamaterials so that all the sealed holes are connected (Fig. 1a). A syringe pump was further connected to the sample as a source of vacuum (Fig. 9a). To measure the pressure in the metamaterials, a manometer (accuracy: ±0.01 kPa) was linked to the syringe via a 'T-shape' connector (Fig. 9a). The deformation of the metamaterials was recorded by a camera and the strains were measured (resolution: 0.01 mm) by tracking the position of the four markers via imaging analysis (Fig. 9b) with the chessboard serving as a reference (Fig. 9a). During the pressure loading, the samples was put on a glass sheet covered by soap water to reduce friction.

Fig. 10 shows the strain–pressure relations for the metamaterials with three sets of geometric parameters same as those in both Figs. 3 and 7: $t/L = 0.05, r/L = 0.475, R/L = 0.475$ for the case 1, $t/L = 0.10, r/L = 0.450, R/L = 0.450$ for the case 2, and $t/L = 0.10, r/L = 0.35, R/L = 0.55$ for the case 3. The experimental results of the critical pressure and the transformation strains show good agreement (Fig. C.1) with those of the simulations (Fig. 3a and b) and the analytical model (Fig. 7a and
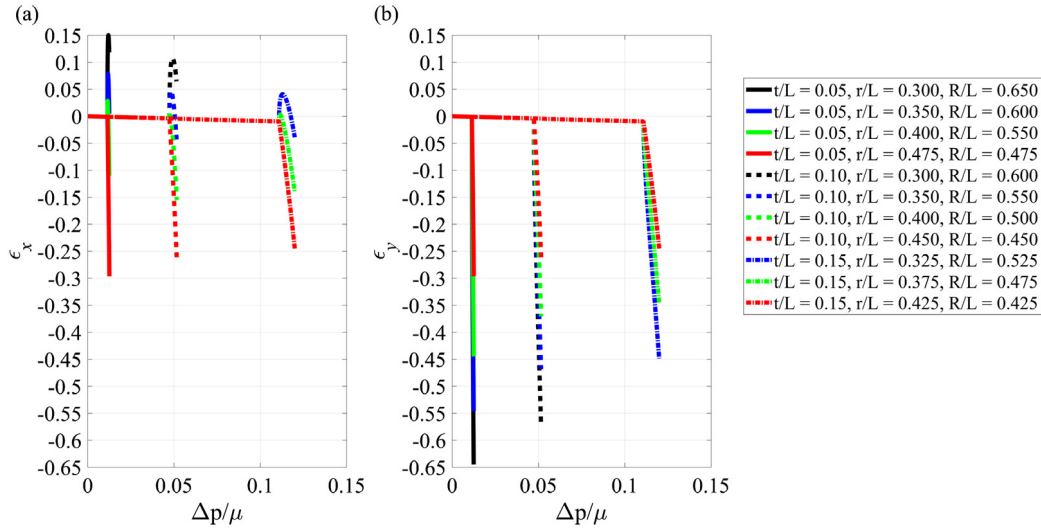
Fig. 8. The dependence of the strains in the (a) x and (b) y directions on the pressure obtained by the analytical model for eleven sets of the geometric parameters. The critical pressure for the onset of the pattern transformation is shown to be governed by the wall thickness.
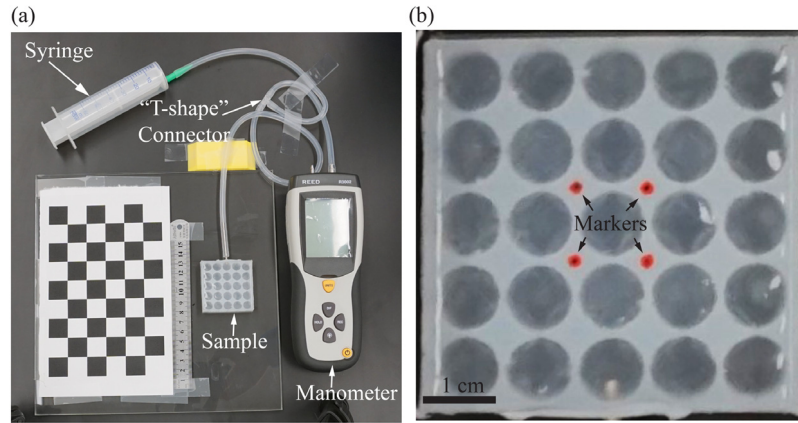
Fig. 9. The setup of the experiments. (a) Top view of the experimental setup. By controlling the amount of air withdrawn from the metamaterials, the internal pressure of the metamaterial can be tuned continuously and measured by a manometer. (b) A camera records the displacement of the markers on the sample to acquire the strains of the metamaterial via imaging analysis. Markers are labeled far away from the boundaries to avoid the boundary effect.
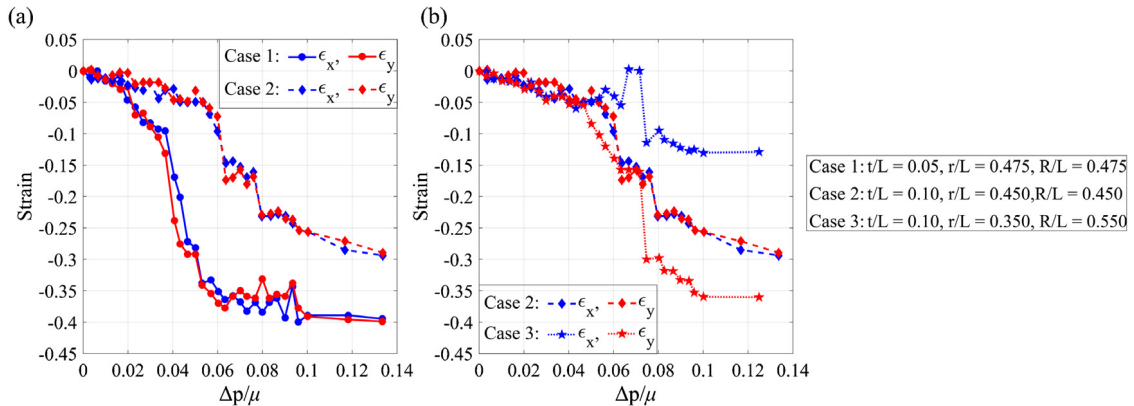
Fig. 10. Experimental results for three metamaterials with geometric parameters exactly same as those shown in Figs. 3 and 7. (a) The strain–pressure curves for the case 1 and case 2. (b) The strain–pressure curves for the case 2 and case 3.

b). They verify the conclusion that the wall thickness governs the critical pressure, and the critical pressure increases with the wall thickness. Although the case 3 has a different pattern of holes from that of the case 2, the critical pressures for the two cases are similar since the wall thicknesses are the same (Fig. 10b). The experiments

also confirm that the pattern of holes controls the transformation strain. The metamaterials with uniform-sized holes in the case 1 and 2 undergo an equibiaxial contraction (Fig. 10a), while the metamaterial with alternatingly large and small holes in the case 3 undergoes a non-equibiaxial contraction (Fig. 10b). Moreover, an

overshoot in $\varepsilon_x - \Delta p$ curve was also observed in the experiment of the case 3 (Fig. 10b), consistent with the simulation (Fig. 3a) and analytical results (Fig. 7a). Note that there are some discrepancies in the strain–pressure curves between the experiments and the simulations (Fig. C.1). Particularly, in the experiment the strain drops at a lower strain than the critical condition for the pattern transformation in the simulation, potentially due to imperfections in the samples, and the strain does not drop as sharply as that in the simulations during the pattern transformation, resulting from the frictions between the metamaterials and the glass sheet.

5. Conclusion

In summary, we numerically, analytically, and experimentally investigate the role of the geometric parameters on the pattern transformation of the metamaterials. We find that the critical pressure for the onset of the pattern transformation is governed by the slenderest wall thickness of the metamaterial, and that the transformation strain is controlled by the pattern of the holes. Our analytical model reveals the mechanics of the pattern transformation and shows good agreement with the finite element analysis. Experimentally, we have achieved pneumatic actuation of the metamaterials and characterized their pattern transformation. The experimental results confirm our theoretical predictions. This study provides design guidelines for the metamaterial and facilitates its real-world applications.

Acknowledgments

Appendix A. Verification of the simplified structures

Here we conduct finite element simulations to verify if the simplified structures shown in Fig. 5b exhibit the similar pattern transformation and strain–pressure curves as their corresponding metamaterials. We convert the three metamaterials in Fig. 3 into their simplified structures with the geometric parameters determined by Eqs. (2)–(5). We simulate the pattern transformation of the three simplified structures under the same pressure load and boundary conditions as shown in Fig. 2b. We model both the deformable beams and rigid rectangles as linear elastic solids, and assign the modulus of the rigid rectangles five order of magnitudes higher than that of the deformable beams so that the deformation in the rigid rectangles is negligible. Eight-node, quadratic, hybrid, plane strain elements (ABAQUS element type CPE8H) are used for the simulation. The results shown in Fig. A.1 agree very well with those in Fig. 3 on the critical pressure and the transformation strains.

Appendix B. Buckling and post-buckling analysis of the equivalent beam structure

Here we briefly derive the buckling condition and the post-buckling process of a beam fixed to two rigid bars under an axial load (Fig. 6a), according to Euler's elastica and the theory of elastic stability [37]. Consider the beam to be inextensible and linearly elastic. The lengths of the beam and each rigid bar are respectively $l_s = 2h$ and $l_r = (L - l_s)/2$. The whole structure is simply supported at the two ends and axially compressed by a force N under the plane strain condition. When the force is large enough, the beam will buckle and deflect from its straight position. The potential energy of this system is given by

$$P[v; N] = \int_0^{l_s} \frac{1}{2} K\varphi'^2 dx - N\Delta L = \int_0^{l_s} \frac{1}{2} K \frac{v''^2}{1 - v'^2} dx - N\Delta L, \text{ (B.1)}$$

where v denotes the deflection of the beam, φ denotes the bending angle, φ' denotes the curvature of the beam, ΔL denotes the length change of the whole structure in the vertical direction, and $K = Ew^3/[12(1 - v^2)]$ is the bending stiffness of the beam under the plain strain condition with E the Young's modulus and v the Poisson's ratio. The coordinate x is chosen to be along the tangential direction of the beam (Fig. 6a), and $v' = dv/dx$ and $v'' = d^2v/dx^2$ are the first and second derivatives of v with respect to x. The length change of the whole structure in the vertical direction ΔL involves the contributions from the beam and the rigid bars, which yields

$$\Delta L = \int_0^{l_s} \left(1 - \sqrt{1 - v'^2}\right) dx + l_r \left(1 - \sqrt{1 - v'(0)^2}\right) + l_r \left(1 - \sqrt{1 - v'(l_s)^2}\right). \tag{B.2}$$

Taylor expanding Eq. (B.1) and neglecting the higher-order terms, we may rewrite the equation as

$$P[v; N] = P_2[v; N] + P_3[v; N] + P_4[v; N], \tag{B.3}$$

where

$$P_2[v; N] = \int_0^{l_s} \left(\frac{1}{2} Kv''^2 - \frac{1}{2} Nv'^2\right) dx - \frac{1}{2} Nl_r v'(0)^2 - \frac{1}{2} Nl_r v'(l_s)^2, \tag{B.4a}$$

$$P_3[v; N] = 0, \tag{B.4b}$$

$$P_4[v; N] = \int_0^{l_s} \left(\frac{1}{2} Kv''^2 v'^2 - \frac{1}{8} Nv'^4\right) dx - \frac{1}{8} Nl_r v'(0)^4 - \frac{1}{8} Nl_r v'(l_s)^4, \tag{B.4c}$$

are the second, third and fourth order terms, respectively.

To establish the governing equations of buckling behavior, the total potential energy $P[v; N]$ must be minimized under the given boundary conditions. It is usually sufficient to minimize only $P_2[v; N]$. Computing the first variation of $P_2[v; N]$ and setting $\delta P_2 = 0$ yields

$$\delta P_2 = 0$$
$$= \int_0^{l_s} \left(Kv'' \delta v'' - Nv' \delta v'\right) dx - Nl_r \left(v'(0) \delta v'(0) + v'(l_s) \delta v'(l_s)\right). \tag{B.5}$$
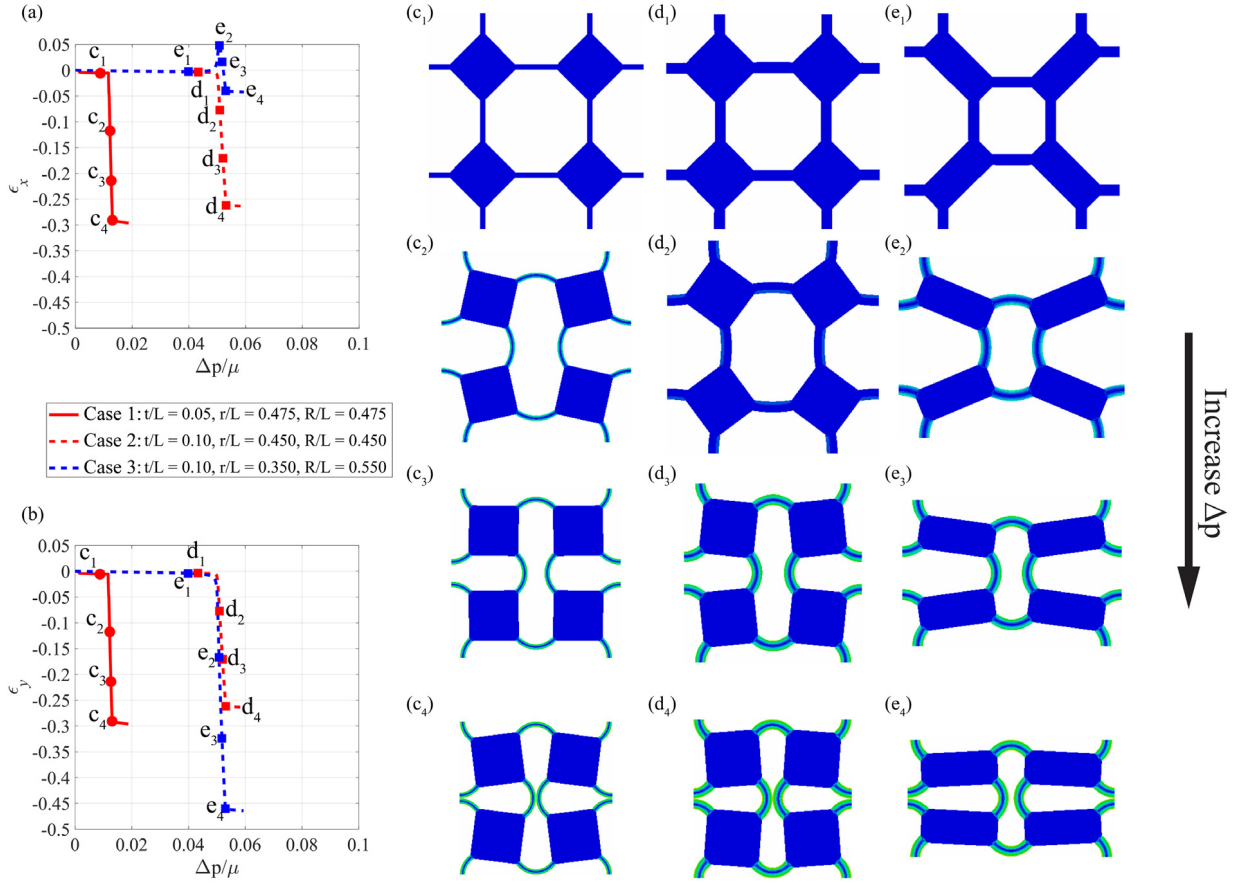
Integration by parts yields

$$\int_0^{l_s} \left(Kv^{(iv)} + Nv''\right) \delta v \, dx + Kv'' \delta v' \Big|_0^{l_s} - \left(Kv''' + Nv'\right) \delta v \Big|_0^{l_s} - Nl_r \left(v'(0) \delta v'(0) + v'(l_s) \delta v'(l_s)\right) = 0, \tag{B.6}$$

from the first term of which we get the Euler–Lagrange equation

$$Kv^{(iv)} + Nv'' = 0. \tag{B.7}$$

Inserting the kinematic boundary conditions, which correspond to the equal bending angles of the beam and the rigid bars at the fixed boundaries (Fig. B.1)

$$\begin{cases} \dfrac{v(0)}{l_r} = v'(0), \\ \dfrac{v(l_s)}{l_r} = -v'(l_s), \end{cases} \tag{B.8}$$

Fig. A.1. The results of finite element simulations to verifying the simplified structures. The dependence of the strains in the (a) x and (b) y directions on the pressure. (c)–(e) The deformed shapes of four unit cells of the three metamaterials: (c) uniformly large holes ($r/L = R/L = 0.475$, $t/L = 0.05$), (d) uniformly small holes ($r/L = R/L = 0.450$, $t/L = 0.10$), and (e) alternantly large and small holes ($r/L = 0.350$, $R/L = 0.550$, $t/L = 0.10$). For each case, the states of deformation correspond to the four selected points on its strain–pressure curves.

into the boundary terms in Eq. (B.6), we can further obtain the static boundary conditions

$$\begin{cases} Kv''(0) = Kv'''(0)\, l_r, \\ Kv''(l_s) + Kv'''(l_s)\, l_r = 0. \end{cases} \tag{B.9}$$

These static boundary conditions correspond to the moment balance about the two pinned joints at the end of the structure (Fig. B.1a, c–d),

$$\begin{cases} M(0) - V(0)\, l_r \cos[\varphi(0)] - Nv(0) = 0, \\ -M(l_s) - V(l_s)\, l_r \cos[\varphi(0)] + Nv(l_s) = 0, \end{cases} \tag{B.10}$$

where M and V are the bending moment and shear force, respectively. Using the relation between M and V obtained by the moment equilibrium of an infinitesimal segment (Fig. B.1c):
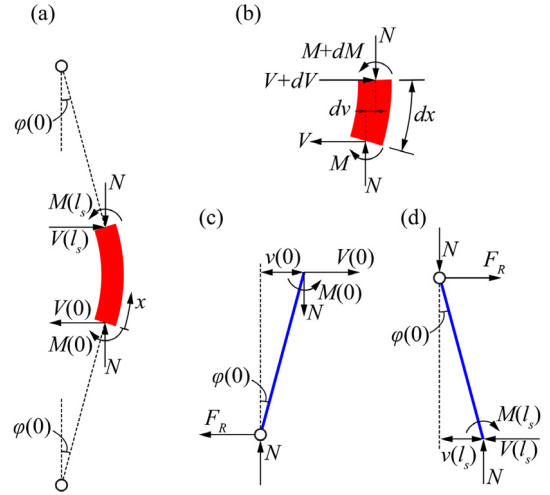
$$M' - Nv' = V \cos \varphi, \tag{B.11}$$

and the relation between the moment and curvature $M = -Kv''/\sqrt{1 - v'^2}$, Eq. (B.10) can recover Eq. (B.9) with the terms higher than the second order neglected.

The general solution to Eq. (B.7) is

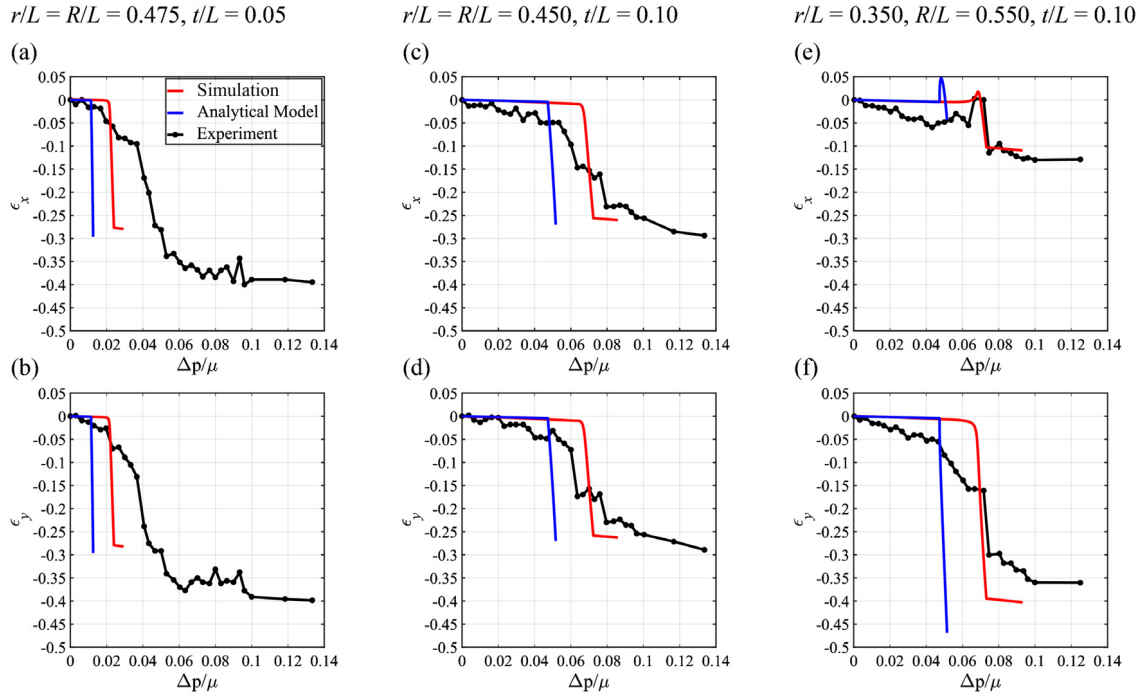$$v(x) = A \sin kx + B \cos kx + Cx + D, \tag{B.12}$$

in which A, B, C, and D are arbitrary constants and k^2 equals N/K. Plug the general solution, Eq. (B.12), into the boundary conditions,

Fig. B.1. Free body diagrams of (a) the beam, (b) an infinitesimal segment of the beam, and (c, d) the two rigid bars.

Eqs. (B.8) and (B.9), and we get

$$\begin{cases} kl_r A - B + l_r C - D = 0, \\ (\sin kl_s + kl_r \cos kl_s)\, A + (\cos kl_s - kl_r \sin kl_s)\, B + (l_s + l_r)\, C + D = 0, \\ kl_r A - B = 0, \\ (\sin kl_s + kl_r \cos kl_s)\, A + (\cos kl_s - kl_r \sin kl_s)\, B = 0. \end{cases} \tag{B.13}$$

Fig. C.1. The dependence of the strains in the (a, c, e) x and (b, d, f) y directions on the pressure for three metamaterials with different geometric parameters: (a, b) uniformly large holes ($r/L = R/L = 0.475$, $t/L = 0.05$), (c, d) uniformly small holes ($r/L = R/L = 0.450$, $t/L = 0.10$), and (e, f) alternatingly large and small holes ($r/L = 0.350$, $R/L = 0.550$, $t/L = 0.10$). The results from the finite element simulations (red), analytical model (blue), and experiments (black) reveal the same effect of the geometric parameters on the pattern transformation of metamaterials. (For interpretation of the references to color in this figure legend, the reader is referred to the web version of this article.)

This algebraic equation system can be rewritten as $\mathbf{M}\begin{bmatrix} A & B & C & D \end{bmatrix}^T = 0$. The constants A, B, C, and D have nonzero solutions only when the determinant of the coefficient matrix $\mathbf{M}$ vanishes, $\det(\mathbf{M}) = 0$, which yields

$$2kl_r \cos kl_s = \left(k^2 l_r^2 - 1\right) \sin kl_s. \tag{B.14}$$

Eq. (B.14) can be numerically solved, and the smallest positive root k_{cr} corresponds to the smallest critical load $N_{cr} = k_{cr}^2 K$. Note that the critical force N_{cr} recovers that of a simply supported beam when $l_r = 0$. A non-zero l_r can significantly reduce the critical buckling force of this equivalent structure of a beam fixed to two rigid bars. The deflections of the buckled beam can be obtained by eliminating B, C and D in Eq. (B.12), which yields

$$v(x) = a \sin(k_{cr}x + \gamma), \tag{B.15}$$

where $a = A\sqrt{k_{cr}^2 l_r^2 + 1}$ is the amplitude of the first buckling mode, and $\tan \gamma = k_{cr}l_r$.

Next, let us consider the post-buckling behavior of the beam when the load N slightly exceeds the critical load N_{cr}. We expand the potential energy $P[v; N]$ in Eq. (B.1) with respect to the load N near $N = N_{cr}$,

$$P[v; N] = P_2[v; N_{cr}] + (N - N_{cr})\dot{P}_2[v; N_{cr}] + P_4[v; N_{cr}], \tag{B.16}$$

where $\dot{()} = \partial/\partial N$ and the terms higher than the fourth order have been neglected. The first term on the right-hand side of Eq. (B.16) vanishes due to the equilibrium, and the potential energy now becomes

$$P[v; N] = (N - N_{cr})\dot{P}_2[v; N_{cr}] + P_4[v; N_{cr}]. \tag{B.17}$$

Using Eqs. (B.15) and (B.4), we can express $\dot{P}_2[v; N_{cr}]$ and $P_4[v; N_{cr}]$ as

$$\dot{P}_2[a; N_{cr}] = -\frac{a^2 k_{cr}^2 \left[l_s\left(1 + k_{cr}^2 l_r^2\right) + 2l_r\right]}{4\left(1 + k_{cr}^2 l_r^2\right)}, \tag{B.18a}$$

$$P_4[a; N_{cr}] = a^4 k_{cr}^4 N_{cr} \frac{l_s\left(1 + k_{cr}^2 l_r^2\right)^2 + 2l_r\left(1 - k_{cr}^2 l_r^2\right)}{64\left(1 + k_{cr}^2 l_r^2\right)^2}. \tag{B.18b}$$

The amplitude of the first buckling mode a can be achieved by minimizing the potential energy with respect to a, $\partial P/\partial a = 0$,

$$a = \frac{1}{2k_{cr}}\sqrt{\frac{N - N_{cr}}{N_{cr}} \frac{32l_s\left(1 + k_{cr}^2 l_r^2\right)^2 + 64l_r\left(1 + k_{cr}^2 l_r^2\right)}{l_s\left(1 + k_{cr}^2 l_r^2\right)^2 + 2l_r\left(1 - k_{cr}^2 l_r^2\right)}}. \tag{B.19}$$

The axial displacement of the beam Δl_s can be calculated as

$$\Delta l_s = \int_0^{l_s}\left(1 - \sqrt{1 - v'^2}\right)dx \approx \int_0^{l_s}\frac{1}{2}v'^2 dx$$
$$= \frac{a^2 k_{cr}^2 \left(l_s + k_{cr}^2 l_r^2 l_s - 2l_r\right)}{4\left(1 + k_{cr}^2 l_r^2\right)}. \tag{B.20}$$

The bending angle $\varphi(x)$ can be calculated as

$$\varphi(x) = \sin^{-1}\left(v'(x)\right) = \sin^{-1}\left(ak_{cr}\cos(k_{cr}x + \gamma)\right). \tag{B.21}$$

Appendix C. Comparing results from the finite element simulations, analytical model and experiments

The results of the strain-pressure curves from simulations, analytical model and experiments show good agreement (Fig. C.1).

Appendix D. Videos

Supplementary material related to this article can be found online at https://doi.org/10.1016/j.eml.2018.08.001.

References

[1] A.A. Zadpoor, Mechanical meta-materials, Mater. Horizons 3 (2016) 371–381. http://dx.doi.org/10.1039/c6mh00065g.

[2] X. Yu, J. Zhou, H. Liang, Z. Jiang, L. Wu, Mechanical metamaterials associated with stiffness, rigidity and compressibility: A brief review, Prog. Mater. Sci. 94 (2018) 114–173. http://dx.doi.org/10.1016/j.pmatsci.2017.12.003.

[3] E.A.R. Ch, Ultralight, ultrastiff mechanical metamaterials, Science 344 (2014) 1373–1378.

[4] L.R. Meza, S. Das, J.R. Greer, Strong, lightweight, and recoverable three-dimensional ceramic nanolattices, Science 345 (2014) 1322–1326. http://dx.doi.org/10.1126/science.1255908.

[5] M. Kadic, T. Bückmann, N. Stenger, M. Thiel, M. Wegener, On the practicability of pentamode mechanical metamaterials, Appl. Phys. Lett. 100 (2012) 191901. http://dx.doi.org/10.1063/1.4709436.

[6] G.W. Milton, A.V. Cherkaev, Which elasticity tensors are realizable? J. Eng. Mater. Technol. 117 (1995) 483–493. http://dx.doi.org/10.1115/1.2804743.

[7] T. Bückmann, M. Kadic, R. Schittny, M. Wegener, Mechanical metamaterials with anisotropic and negative effective mass-density tensor made from one constituent material, Phys. Status Solidi 252 (2015) 1671–1674.

[8] R.S. Lakes, Foam structures with a negative Poisson's ratio, Science 235 (1987) 1038–1040. http://dx.doi.org/10.1126/science.235.4792.1038.

[9] G.W. Milton, Composite materials with Poisson's ratios close to - 1, J. Mech. Phys. Solids 40 (1992) 1105–1137. http://dx.doi.org/10.1016/0022-5096(92)90063-8.

[10] J.N. Grima, K.E. Evans, Auxetic behavior from rotating squares, J. Mater. Sci. Lett. 19 (2000) 1563–1565. http://dx.doi.org/10.1023/A:1006781224002.

[11] K. Bertoldi, P.M. Reis, S. Willshaw, T. Mullin, Negative Poisson's ratio behavior induced by an elastic instability, Adv. Mater. 22 (2010) 361–366. http://dx.doi.org/10.1002/adma.200901956.

[12] G.N. Greaves, A.L. Greer, R.S. Lakes, T. Rouxel, Poisson's ratio and modern materials (vol 10, pg 823, 2011), Nature Mater. 10 (2011) 986. http://dx.doi.org/10.1038/nmat3177.

[13] J. Shim, C. Perdigou, E.R. Chen, K. Bertoldi, P.M. Reis, Buckling-induced encapsulation of structured elastic shells under pressure, Proc. Natl. Acad. Sci. 109 (2012) 5978–5983. http://dx.doi.org/10.1073/pnas.1115674109.

[14] K. Sun, A. Souslov, X. Mao, T.C. Lubensky, Isostaticity, auxetic response, surface modes, and conformal invariance in twisted kagome lattices, Proc. Natl. Acad. Sci. 109 (2011) 12369–12374. http://dx.doi.org/10.1073/pnas.1119941109.

[15] L. Mizzi, K.M. Azzopardi, D. Attard, J.N. Grima, R. Gatt, Auxetic metamaterials exhibiting giant negative Poisson's ratios, Phys. Status Solidi - Rapid Res. Lett. 9 (2015) 425–430. http://dx.doi.org/10.1002/pssr.201510178.

[16] H. Yasuda, J. Yang, Reentrant origami-based metamaterials with negative Poisson's ratio and bistability, Phys. Rev. Lett. 114 (2015) 185502. http://dx.doi.org/10.1103/PhysRevLett.114.185502.

[17] A. Rafsanjani, A. Akbarzadeh, D. Pasini, Snapping mechanical metamaterials under tension, Adv. Mater. 27 (2015) 5931–5935. http://dx.doi.org/10.1002/adma.201502809.

[18] D. Restrepo, N.D. Mankame, P.D. Zavattieri, Phase transforming cellular materials, Extrem. Mech. Lett. 4 (2015) 52–60. http://dx.doi.org/10.1016/j.eml.2015.08.001.

[19] A. Rafsanjani, D. Pasini, Bistable auxetic mechanical metamaterials inspired by ancient geometric motifs, Extrem. Mech. Lett. 9 (2016) 291–296. http://dx.doi.org/10.1016/j.eml.2016.09.001.

[20] T. Frenzel, M. Kadic, M. Wegener, Three-dimensional mechanical metamaterials with a twist, Science 358 (2017) 1072–1074. http://dx.doi.org/10.1126/science.aao4640.

[21] T. Mullin, S. Deschanel, K. Bertoldi, M.C. Boyce, Pattern transformation triggered by deformation, Phys. Rev. Lett. 99 (2007) 84301. http://dx.doi.org/10.1103/PhysRevLett.99.084301.

[22] K. Bertoldi, M.C. Boyce, S. Deschanel, S.M. Prange, T. Mullin, Mechanics of deformation-triggered pattern transformations and superelastic behavior in periodic elastomeric structures, J. Mech. Phys. Solids 56 (2008) 2642–2668. http://dx.doi.org/10.1016/j.jmps.2008.03.006.

[23] J. Shim, S. Shan, A. Košmrlj, S.H. Kang, E.R. Chen, J.C. Weaver, K. Bertoldi, Harnessing instabilities for design of soft reconfigurable auxetic/chiral materials, Soft Matter 9 (2013) 8198–8202. http://dx.doi.org/10.1039/c3sm51148k.

[24] B. Florijn, C. Coulais, M. van Hecke, Programmable mechanical metamaterials, Phys. Rev. Lett. 113 (2014) 175503.

[25] J.T.B. Overvelde, K. Bertoldi, Relating pore shape to the non-linear response of periodic elastomeric structures, J. Mech. Phys. Solids 64 (2014) 351–366.

[26] B. Florijn, C. Coulais, M. van Hecke, Programmable mechanical metamaterials: The role of geometry, Soft Matter 12 (2016) 8736–8743.

[27] G. Wang, M. Li, J. Zhou, Switching of deformation modes in soft mechanical metamaterials, Soft Mater 14 (2016) 180–186.

[28] D. Yang, L. Jin, R.V. Martinez, K. Bertoldi, G.M. Whitesides, Z. Suo, Phase-transforming and switchable metamaterials, Extrem. Mech. Lett. 6 (2016) 1–9.

[29] D. Yang, B. Mosadegh, A. Ainla, B. Lee, F. Khashai, Z. Suo, K. Bertoldi, G.M. Whitesides, Buckling of elastomeric beams enables actuation of soft machines, Adv. Mater. 27 (2015) 6323–6327. http://dx.doi.org/10.1002/adma.201503188.

[30] K. Bertoldi, M.C. Boyce, Mechanically triggered transformations of phononic band gaps in periodic elastomeric structures, Phys. Rev. B 77 (2008) 52105.

[31] K. Bertoldi, Harnessing instabilities to design tunable architected cellular materials, Annu. Rev. Mater. Res. 47 (2017) 51–61. http://dx.doi.org/10.1146/annurev-matsci-070616-123908.

[32] C.G. Johnson, U. Jain, A.L. Hazel, D. Pihler-Puzović, T. Mullin, On the buckling of an elastic holey column, Proc. R. Soc. A 473 (2017) 20170477.

[33] Y. He, Y. Zhou, Z. Liu, K.M. Liew, Pattern transformation of single-material and composite periodic cellular structures, Mater. Des. 132 (2017) 375–384.

[34] P. Wang, J. Shim, K. Bertoldi, Effects of geometric and material nonlinearities on tunable band gaps and low-frequency directionality of phononic crystals, Phys. Rev. B 88 (2013) 14304.

[35] R.W. Ogden, Non-Linear Elastic Deformations, Courier Corporation, 1984. http://dx.doi.org/10.1016/0264-682X(84)90061-3.

[36] M.C. Boyce, E.M. Arruda, Constitutive models of rubber elasticity: A review, Rubber Chem. Technol. 73 (2000) 504–523. http://dx.doi.org/10.5254/1.3547602.

[37] W.T. Koiter, Elastic Stability of Solids and Structures, Cambridge University Press Cambridge, 2008. http://dx.doi.org/10.1017/CBO9780511546174.

[38] C. Coulais, J.T.B. Overvelde, L.A. Lubbers, K. Bertoldi, M. Van Hecke, Discontinuous buckling of wide beams and metabeams, Phys. Rev. Lett. 115 (2015) 044301. http://dx.doi.org/10.1103/PhysRevLett.115.044301.

[39] R.V. Martinez, J.L. Branch, C.R. Fish, L. Jin, R.F. Shepherd, R.M.D. Nunes, Z. Suo, G.M. Whitesides, Robotic tentacles with three-dimensional mobility based on flexible elastomers, Adv. Mater. 25 (2013) 205–212. http://dx.doi.org/10.1002/adma.201203002.